Tsukahara et al. *NPG Asia Materials* (2020) 12:29
https://doi.org/10.1038/s41427-020-0210-2

NPG Asia Materials

ARTICLE Open Access

Relationship between magnetic nucleation and the microstructure of a hot-deformed permanent magnet: micromagnetic simulation

Hiroshi Tsukahara[1], Kaoru Iwano[1], Tadashi Ishikawa[1], Chiharu Mitsumata[2] and Kanta Ono[1]

Abstract

The grains initiating magnetization reversal in the microstructure of a hot-deformed permanent magnet have been identified in this study by performing micromagnetic simulations based on the Landau–Lifshitz–Gilbert equation. Hot-deformed permanent magnets comprise tabular grains, the easy-axis orientations of which are inclined with respect to the nominal easy axis of the permanent magnet. In the simulation model, the grains complexly overlap, similar to in actual permanent magnets. We analyze the simulation results considering grain overlap and the easy-axis tilt angles of the grains. The initiation of magnetic nucleation requires a high concentration of grains with large easy-axis tilt angles. We clarify the magnetic-nucleation process and provide a method to enhance the performance of permanent magnets by avoiding a high concentration of grains with large easy-axis tilt angles.

Introduction

Control of magnetization reversal enables us to improve the performance of permanent magnets, which are indispensable for high-efficiency motors. Hot-deformed permanent magnets are candidate materials with high coercivity that do not contain heavy rare earth elements[1–4]. Hot-deformed permanent magnets consist of tabular grains whose diameter and thickness are on the submicron and nanometer order, respectively[5–9]. A permanent magnet must have high coercivity to resist the alternating magnetic field generated in a motor. However, the coercivity of a realistic permanent magnet is smaller than that suggested by micromagnetics theory[10]. Magnetic nucleation and domain wall motion reduce the coercivity. When the external magnetic field approaches the coercivity, the magnetization starts to be reversed in tabular grains, and the domain walls move into the other grains[11–15]. Although the origins of magnetization reversal have been theoretically and experimentally investigated, it remains to be clarified how magnetization reversal is nucleated inside a permanent magnet[16–19]. The purpose of this study is to identify the relationship between magnetization reversal and the microstructure of a permanent magnet.

The region of magnetization reversal inside permanent magnets expands during demagnetization. Both magnetic nucleation and domain wall motion change the magnetization owing to exchange and dipolar interactions. The dipole field is generated by the magnetization of all grains in the permanent magnet, in which the grains complexly overlap. To understand the mechanism of the magnetization reversal process, one must consider the microstructures of permanent magnets such as the diameter, easy-axis tilt, and grain overlap.

The coercivity and magnetic nucleation of permanent magnets have been extensively investigated[20–25]. The coercivity of sintered permanent magnets has been revealed using the isolated grain model with scalar parameters that represent the effects of the magnetization of other grains[26–29]. The orientation of the magnetization direction inside grains is driven by the dipole field, which also induces magnetic nucleation at grain corners[30,31]. However, the effect of permanent magnet microstructures on the initiation of magnetic

Correspondence: Kanta Ono (kanta.ono@kek.jp)
[1]High Energy Accelerator Research Organization (KEK), Tsukuba, Ibaraki 305-0801, Japan
[2]National Institute for Materials Science (NIMS), Tsukuba 305-0047, Japan

© The Author(s) 2020
Open Access This article is licensed under a Creative Commons Attribution 4.0 International License, which permits use, sharing, adaptation, distribution and reproduction in any medium or format, as long as you give appropriate credit to the original author(s) and the source, provide a link to the Creative Commons license, and indicate if changes were made. The images or other third party material in this article are included in the article's Creative Commons license, unless indicated otherwise in a credit line to the material. If material is not included in the article's Creative Commons license and your intended use is not permitted by statutory regulation or exceeds the permitted use, you will need to obtain permission directly from the copyright holder. To view a copy of this license, visit http://creativecommons.org/licenses/by/4.0/.

nucleation is yet to be completely understood. To investigate the interplay between the permanent magnet microstructure and magnetic nucleation, large-scale micromagnetic simulations considering a large number of grains must be performed.

In this study, we investigated magnetization reversal inside a permanent magnet during the demagnetization process and the effects of the microstructure of the permanent magnet on the generation of magnetic nucleation using a large-scale micromagnetics simulation based on the Landau–Lifshitz–Gilbert (LLG) equation[32–39]. When the external field approaches the coercivity of the permanent magnet, magnetization reversal is initiated in some grains; the density of the grains undergoing nucleation is small. After nucleation formation, the magnetization reversal begins to propagate inside the permanent magnet through domain wall motion across the grain boundaries. The dipole field has a distribution, and its strength exceeds 1.7 T in some regions where magnetization reversal is initiated. The dipole field does not have a correlation with the permanent magnet microstructure, and the easy-axis orientations identify grains wherein magnetization reversal can be initiated during demagnetization.

Models and methods

We performed a large-scale micromagnetics simulation using the hot-deformed permanent magnet model, as shown in Fig. 1a. The simulation model of 2048 × 2048 × 512 nm^3 contains 3391 tabular gains, whose thicknesses are 32 nm[40]. The grains are randomly placed in the xy-plane and are in contact with each other in both the xy-plane and the z-direction. The model is fabricated by stacking layers of grains. The layers are constructed by a simple molecular dynamics method[40,41]. The distributions of the grain diameters and the easy-axis orientations of each grain are shown in Fig. 1b. The easy-axis tilt angle from the z-direction, $\Delta\theta$, has a von Mises distribution, and the azimuthal angle, ϕ, is oriented along a random direction. We define the grain diameter as $\sqrt{V/\pi d}$, where V and d are the volume and thickness of the grain, respectively. The grain diameter has a Gaussian distribution with a maximum (minimum) value of 189.6 (124.2) nm; the average diameter is 158.4 nm. The average and maximum $\Delta\theta$ are 11.7° and 52.4°, respectively.

The magnetization dynamics is simulated by solving the LLG equation:

$$\frac{d\boldsymbol{m}(\boldsymbol{x})}{dt} = -\gamma \boldsymbol{m}(\boldsymbol{x}) \times \boldsymbol{H}_{\mathrm{eff}}(\boldsymbol{x}) + \alpha \boldsymbol{m}(\boldsymbol{x}) \times \frac{d\boldsymbol{m}(\boldsymbol{x})}{dt}, \quad (1)$$

where $\boldsymbol{x}$ is a position vector, $\boldsymbol{m}(\boldsymbol{x})$ is the normalized magnetization, α is the Gilbert damping constant, γ is the gyromagnetic ratio, and $\boldsymbol{H}_{\mathrm{eff}}(\boldsymbol{x})$ is the effective field. In this study, the effective field consists of the external, $\boldsymbol{H}_{\mathrm{ext}}(\boldsymbol{x})$, dipole, $\boldsymbol{H}_{\mathrm{dip}}(\boldsymbol{x})$, exchange, $\boldsymbol{H}_{\mathrm{exc}}(\boldsymbol{x})$, and anisotropy, $\boldsymbol{H}_{\mathrm{ani}}(\boldsymbol{x})$, fields. The exchange and anisotropy fields are described by:

$$\boldsymbol{H}_{\mathrm{exc}}(\boldsymbol{x}) = \frac{2}{\mu_0 M_s} \nabla \cdot [A(\boldsymbol{x}) \nabla \boldsymbol{m}(\boldsymbol{x})], \quad (2)$$

$$\boldsymbol{H}_{\mathrm{ani}}(\boldsymbol{x}) = \frac{2K_{1u}}{\mu_0 M_s} [\boldsymbol{m}(\boldsymbol{x}) \cdot \hat{\boldsymbol{e}}_a(\boldsymbol{x})] \hat{\boldsymbol{e}}_a, \quad (3)$$

where $A(\boldsymbol{x})$ is the exchange stiffness constant, M_s is the saturation magnetization, K_{1u} is the uniaxial anisotropy constant, and $\hat{\boldsymbol{e}}_a$ is the easy axis[42–45]. The simulation model is segmented into 268,435,456 cubic cells of dimensions 2.0 × 2.0 × 2.0 nm^3 to simulate the magnetization dynamics using the finite-difference method under periodic boundary conditions. After discretization, the dipole field is obtained by:

$$\boldsymbol{H}_{\mathrm{dip}}(\boldsymbol{x}_i) = M_s \sum_j \sum_{\xi} K(\boldsymbol{x}_i - \boldsymbol{x}_j + \boldsymbol{\xi}) \boldsymbol{m}(\boldsymbol{x}_j), \quad (4)$$

where $\boldsymbol{x}_i$ represents the center of the ith cell inside one period, $K(\boldsymbol{x}_i - \boldsymbol{x}_j + \boldsymbol{\xi})$ is the demagnetization tensor[44],

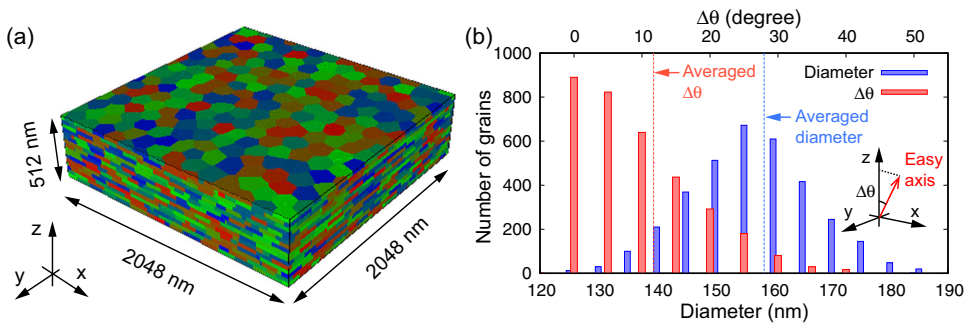

Fig. 1 Structure of simulation model. a Simulation model for the hot-deformed permanent magnet of 2048 × 2048 × 512 nm^3[40]. Each tabular grain region is indicated by a different color. **b** Distributions of the diameters and the easy-axis tilt angles. Blue (red) indicates the number of grains as a function of the diameter (easy-axis tilt angle $\Delta\theta$) of the individual grains. $\Delta\theta$ is defined in the inset of **b**.

and $\boldsymbol{\xi}$ is the displacement vector of the periodic system. The displacement vector is represented by $\boldsymbol{\xi} = (L_x n_x, L_y n_y, L_z n_z)$, where L_l is the system length in the l-direction, and n_l is an integer. We set the cutoff of the sum of the demagnetization tensor to three periods. Thus, n_l varies from -1 to 1. We parallelize the simulation using the message passing interface. We perform data transfer for stencil and fast Fourier transformation, which are essential for the calculation of the exchange and dipole fields, respectively[46]. We adopt the Runge–Kutta–Fehlberg method with an adjustable time step for the time evolution of the magnetization[47]. We employ the fourth- and fifth-order Runge–Kutta methods for the time evolution of the magnetization and the error ratio, respectively (RKF45). The accuracy of the time evolution and the safety factor are set to 1.0×10^{-4} and 0.95, respectively[48]. The external field is changed with a step of 0.2 T to obtain a demagnetization curve. The magnetization is relaxed at each step until the average torque is $1.0 \times 10^{-3}\,\mathrm{s}^{-1}$.

We assume that the magnetic material of the grain is $Nd_2Fe_{14}B$, whose parameters are as follows[49–54]: $\mu_0 M_s = 1.61$ T, $K_{1u} = 4.5 \times 10^6\,\mathrm{J/m^3}$, $\alpha = 1.0$, and $|\gamma| = 1.76 \times 10^7\,\mathrm{s^{-1}G^{-1}}$. We set the exchange stiffness constant, $A(\boldsymbol{x})$, to 1.25×10^{-11} J/m for intragrain exchange interactions. In this study, we consider the thin-limit grain boundary phase without crystalline anisotropy. When the grain boundary phase becomes infinitely thin, the magnetization of the grain boundary phase does not affect the dipole field. However, the grain boundary phase weakens the exchange interaction between the grains. Hence, we set the exchange constant between the grains to 1.25×10^{-13} J/m. In our previous studies, we reproduced the motion of the domain walls, which stopped at the grain boundaries in the initial magnetization process, and the two-step structure of the initial magnetization curve for the hot-deformed permanent magnet using the same treatment as that for the grain boundary phase[40]. The micromagnetic simulation was performed on Blue Gene/Q at the High Energy Accelerator Research Organization in Japan, and we used our own simulator[46,55,56].

Results and discussion

Demagnetization curve and magnetization reversal

A demagnetization curve obtained by the micromagnetics simulation is shown in Fig. 2a. The demagnetization curve shows a high squareness ratio, which is consistent with that obtained in the experiments on the hot-deformed permanent magnet. The coercivity of our simulation model is 2.9 T. Figure 2b shows the magnetization configuration near the coercivity indicated by B in Fig. 2a. When the external field approaches the coercivity, the magnetization has an interaction magnetic domain structure, in which single-domain grains with positive or negative m_z constitute the magnetic domain structure in the xy-plane[39]. Along the z-direction, the magnetization tends to produce columnar structures owing to the dipolar interaction. After the external field reaches -2.8 T, the average magnetization along the z-direction gradually decreases. Figure 2c shows the time evolution of the average m_z when the external field is -2.8 T during the demagnetization process. Initially, the average m_z gradually decreases because nucleation of magnetization reversal occurs in a few regions. After 1.0 ns, the average m_z quickly decreases owing to the expansion of magnetization reversal regions.

Figure 2d–f shows three-dimensional images of the magnetization reversal regions at different times when the external field is -2.8 T. The magnetization reversal regions appear in only three areas when the elapsed time is 0.04 ns. The domain wall displacement, which expands the magnetization reversal region, tends to be stopped at grain boundaries owing to the reduction in the exchange interaction to 1.0% of that inside the grains. In contrast, the dipolar interaction promotes domain wall displacement across the grain boundaries along the z-direction. As a result, the magnetization reversal region produces a pillar-shaped magnetic domain at 0.76 ns owing to the dipole field. This pillar-shaped magnetization reversal region expands in the xy-plane, as shown in Fig. 2f, and finally, the interaction domain structure appears in the permanent magnet[39].

As shown in Fig. 2b, the magnetization is reversed in approximately half of the permanent magnet, even if the magnetization reversal initiates in just a few grains. To clarify the origin of the nucleation of magnetization reversal, we analyzed the magnetization and the effective field of the remanent magnetization states. Figure 3b shows the magnetization in the remanent magnetization states. When the external field is -2.8 T, the magnetization is reversed in the grain with $\Delta\theta = 52.4°$, as shown in Fig. 3a. The magnetization reversal is initiated near the grain boundary because the grain boundary weakens the exchange interaction. A magnetic-nucleation site also occurs near the grain boundary in another magnetization reversal region, as indicated in Fig. 2d. The magnetization tends to be oriented in the same direction inside the grains in the remanent magnetization states. In contrast, the effective field is distributed inside the grains. Figure 3c–e shows the exchange, anisotropy, and dipole fields, which comprise the effective field when the external field is 0.0 T. The exchange and anisotropy fields are uniform in the magnetization reversal regions, as indicated by the arrows in Fig. 3e, and these fields are positive or almost zero inside the grains. In contrast, the dipole field has a nonuniform distribution[57,58] and a negative value in region A; the strength of the dipole field reaches 1.76 T in the z-direction. The total magnetic field approaches

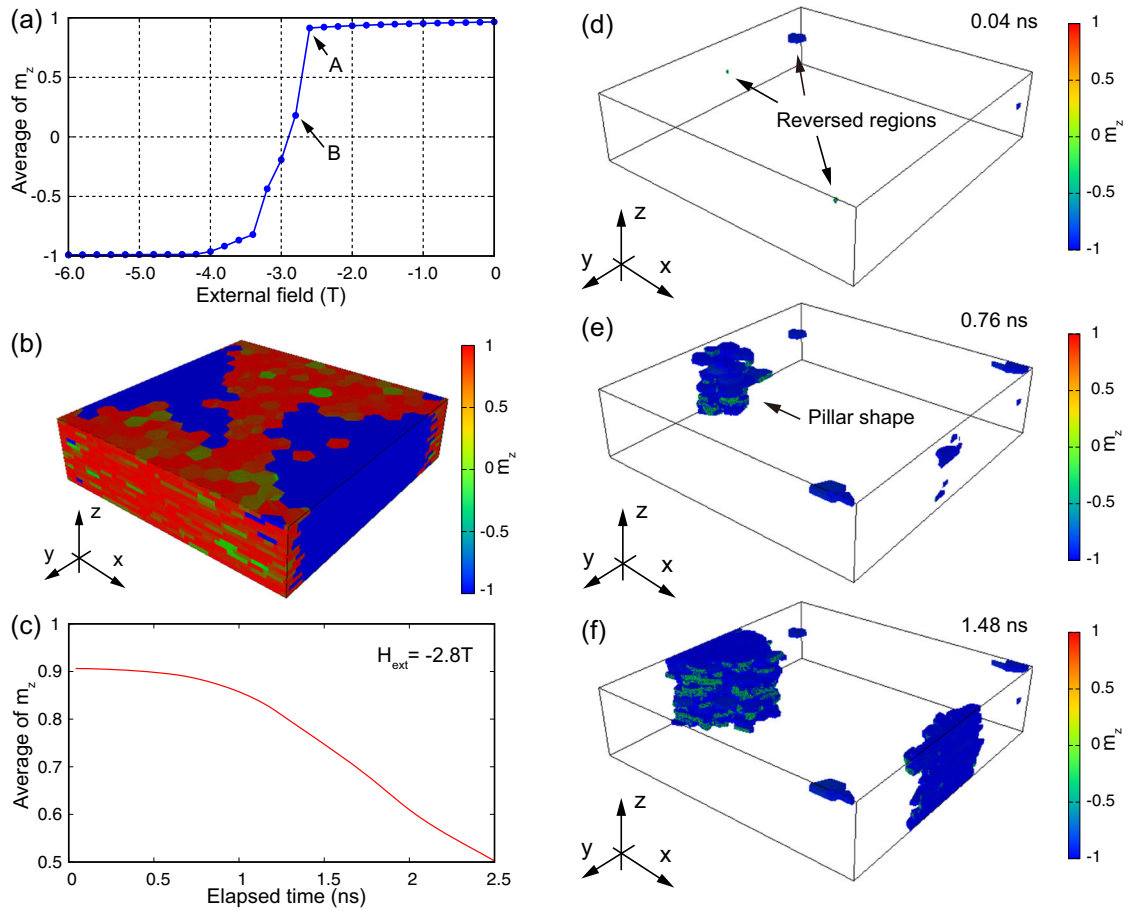

Fig. 2 Magnetization dynamics during demagnetization process. **a** Calculated demagnetization curve; **b** three-dimensional image of magnetization at $H_{ext} = -2.8$ T, in which different values of m_z are represented by different colors[39]; and **c** time evolution of average magnetization along the *z*-direction, which starts from the stable magnetization at $H_{ext} = -2.6$ T, when the external field is −2.8 T. The average m_z at $H_{ext} = -2.6$ and −2.8 T are indicated by A and B in **a**. Snapshots of magnetization reversal regions when the elapsed times are **d** 0.04 ns, **e** 0.76 ns, and **f** 1.48 ns; the external field is −2.8 T. Different values of m_z are represented by different colors. The regions in which m_z has a positive value are transparent.

4.56 T around region A, which exceeds the switching field of this grain. The switching field of a single-domain grain H_c^g is estimated by:

$$H_c^g = \frac{2K_{1u}}{\mu_0 M_s} \frac{1}{\left[(\cos\Delta\theta)^{2/3} + (\sin\Delta\theta)^{2/3}\right]^{3/2}}, \quad (5)$$

which is 3.55 T for the grain in which the magnetization is partially reversed in Fig. 3a[26,59]. Although the dipole field also has a negative value in other regions, the total magnetic field does not exceed the switching field of the grains. The dipole field has a large absolute value at the edges of the grains in neighboring layers.

Relationship between magnetization reversal and microstructure

The dipole field plays an essential role in the realization of magnetization reversal in permanent magnets[30,31]. Fig. 3e shows the application of a strong dipole field to the corner of a grain, initiating magnetization reversal inside the permanent magnet. To illustrate the relationship between magnetization reversal and the permanent magnet microstructure, the dipole field of a simple system comprising two grains, shown in Fig. 4a, was calculated. The easy axis of the single-crystal magnetic material is fixed in the *z*-direction. The grain diameter and thickness are 160.0 and 32 nm, respectively. We independently tilt the easy-axis orientations of the grain ($\Delta\theta_1$) and the contacted grain ($\Delta\theta_2$), and the easy axes of the grain and the contacted grain are tilted in the +x and −x directions, respectively. We assume that the magnetization is orientated parallel to the easy axis. Figure 4b shows the dipole field at the interface between the upper and lower grains when $\Delta\theta_1$ and $\Delta\theta_2$ are 45°. The dipole field has a large value at the edges of the grains, and the absolute value of the dipole field approaches 1.07 T. Figure 4c shows the dipole field at the corner indicated by the gray circle in Fig. 4a as

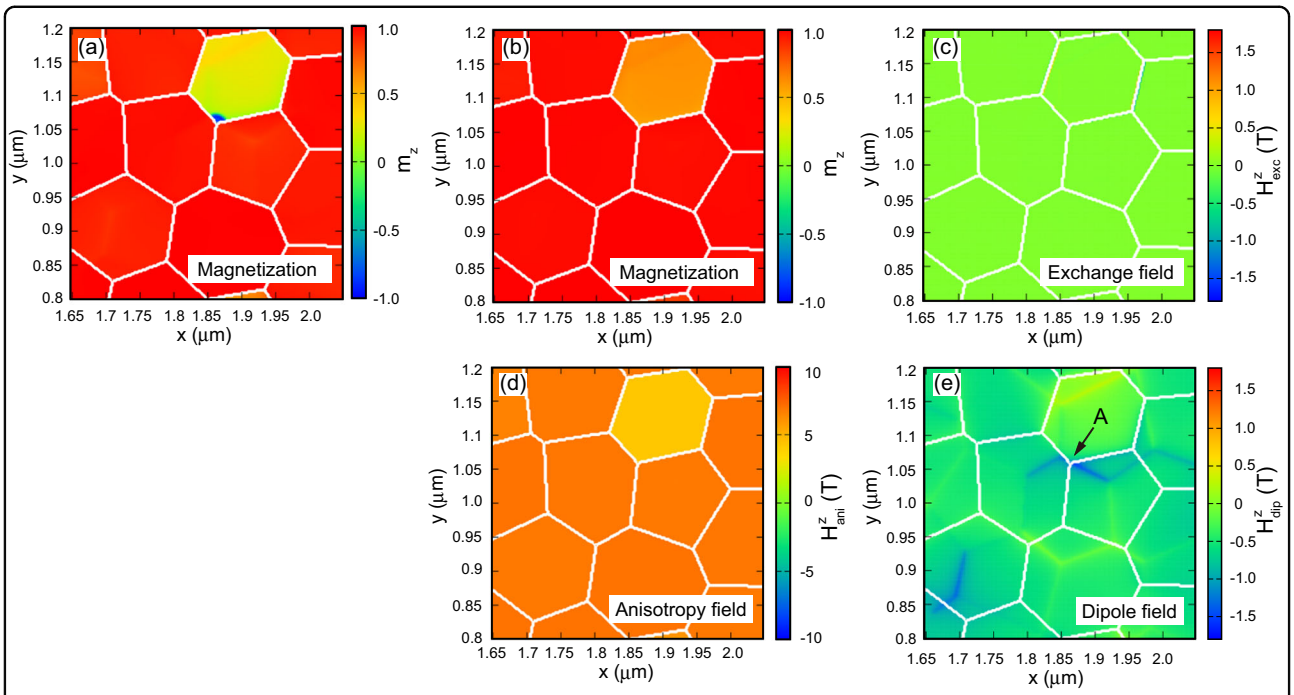

Fig. 3 Magnetizations and magnetic fields. **a** Magnetization configuration around the region where the magnetization starts to be reversed when the external field is −2.8 T. **b** Magnetization configuration, **c** exchange, **d** anisotropy, and **e** dipole fields along the *z*-direction when the external field is 0.0 T.

functions of $\Delta\theta_1$ and $\Delta\theta_2$. The dipole field has a finite value of −0.54 T, even though the easy axes are not tilted. Although the contour lines exhibit curvature with increasing $\Delta\theta_1$ and $\Delta\theta_2$, the dipole field is approximately proportional to $\Delta\theta_1 + \Delta\theta_2$ when $\Delta\theta_1$ and $\Delta\theta_2$ are small. In the following analysis, we consider this rough approximation.

In actual permanent magnets, magnetization produces a nonuniform dipole field because the strong anisotropy field of the grains tilts the magnetization from the *z*-direction. Hence, the values of $\Delta\theta$ concerning contacted grains were calculated to investigate the relationship between the initiation of magnetization and the easy-axis tilt angles. It is noteworthy that the proposed study ignores the effect of the azimuthal angle to simplify the analysis of the simulation results.

To analyze the simulation results with the realistic model, we define $\Delta\theta_{i,1}$ as the largest easy-axis tilt angle among those of the contacted grains in the *z*-direction, as shown in Fig. 4d. Figure 4e shows the relationship between the maximum dipole field along the *z*-direction inside the grains and the tilt angles of the grains, including the contacted grains. We consider the remanent magnetization, and the sign of the dipole field is not considered in this analysis. The dotted line shows the dipole field along the *z*-direction as calculated by the two-grain model with $\Delta\theta_1 = \Delta\theta_2$. The dotted line is located at the center of the distribution of the maximum dipole fields of the grains. The maximum dipole field does not have a correlation with $\Delta\theta_i + \Delta\theta_{i,1}$; the correlation coefficient is 0.33. The colors indicate the switching fields of the grains obtained by Eq. 5. The correlation coefficient r between data sets A_i, and B_i is defined by:

$$r = \frac{\sum_{i=1}^{n}(A_i - \overline{A})(B_i - \overline{B})}{\sqrt{\sum_{i=1}^{n}(A_i - \overline{A})^2}\sqrt{\sum_{i=1}^{n}(B_i - \overline{B})^2}}, \quad (6)$$

where $\overline{A}$ and $\overline{B}$ are the average A_i and B_i, respectively, and n is the data size. When $\Delta\theta_i + \Delta\theta_{i,1}$ exceeds 70.0, a dipole field of over 1.0 T is applied to grains in the *z*-direction, whose switching fields are ~4.0 T. Figure 4f shows the dipole field around grains A and B, which are defined in Fig. 4e. As can be seen, the magnetization within grains A and B enhances the positive dipole field. This positive dipole field is weak because the average dipole field has a negative sign inside permanent magnets. Thus, the dipole field cannot be described only by the easy-axis orientation.

As shown in Fig. 2d–f, the grains have a multidomain structure during the switching process, and finally, the magnetization is completely reversed inside the grains. Hence, we can define the "switching time" of a grain as when the total m_z of the grain is 0. A shorter switching time represents a preference for magnetization reversal. Figure 5 shows the switching time as a function of $\Delta\theta_i + \Delta\theta_{i,1}$. Initially, the magnetization is reversed in the grains with $\Delta\theta_i + \Delta\theta_{i,1} \geq 60.0°$. After that, the domain walls continuously move into the grains with relatively large

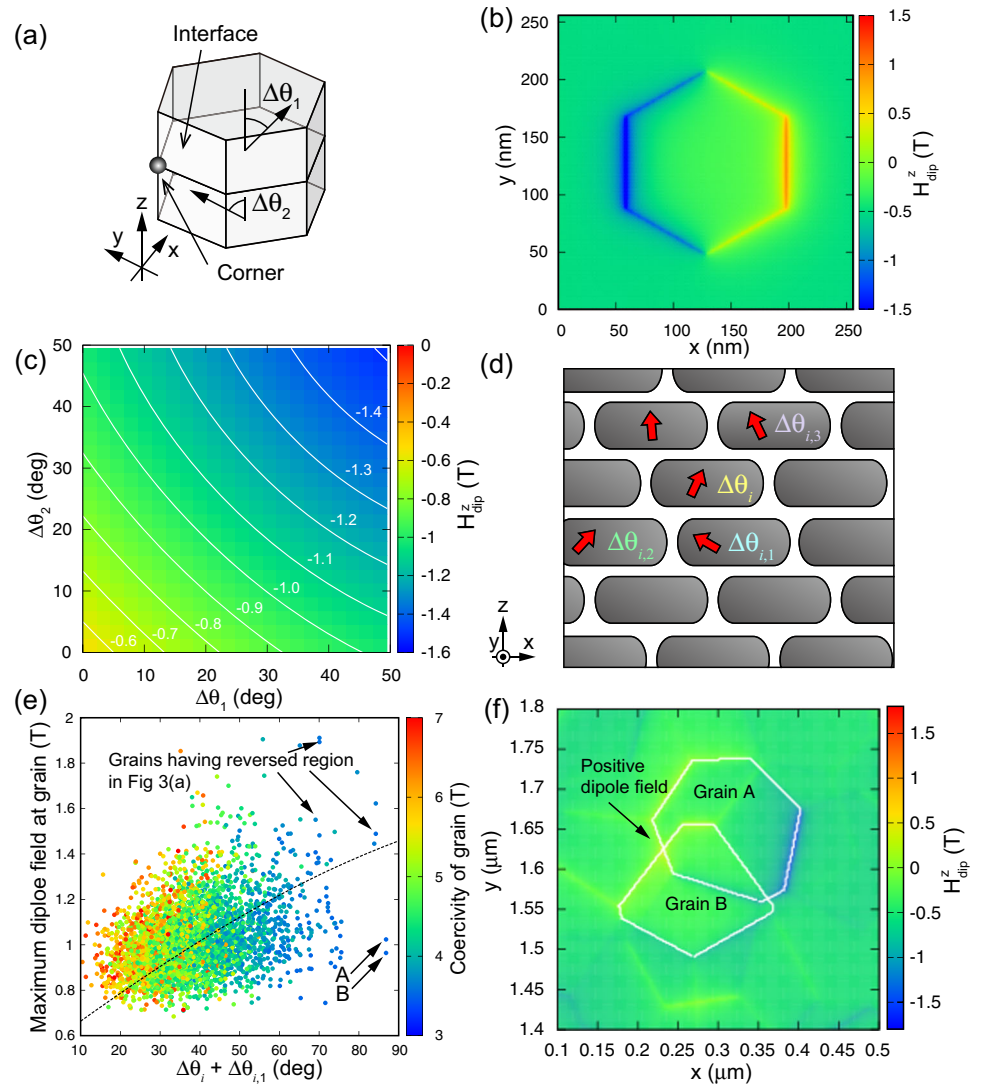

Fig. 4 Relations between dipole fields and microstructures. **a** Schematic of the two-grain model, wherein hexagonal flat grains are stacked along the *z*-direction. **b** Calculated dipole field along the *z*-direction at an interface between two grains. **c** Dipole field as a function of the easy-axis tilt angles of upper ($\Delta\theta_1$) and lower grains ($\Delta\theta_2$). The dipole field along the *z*-direction is indicated by different colors. White colors represent contour lines. **d** Easy-axis tilt angle of a grain ($\Delta\theta_j$). $\Delta\theta_{i,1}$, $\Delta\theta_{i,2}$, and $\Delta\theta_{i,3}$ are the first-, second-, and third-largest easy-axis tilt angles among those of the contacted grains along the *z*-direction, respectively. Gray regions and red arrows represent the grains and the easy-axis orientations, respectively. **e** Relationship between the maximum dipole field along the *z*-direction and $\Delta\theta_i + \Delta\theta_{i,1}$. Colors represent the grain coercivity calculated using Eq. 5. The dotted line represents the relationship between the dipole field of the two-grain model and the tilted angles of the grains. Grains demonstrating regions of magnetization reversal in Fig. 2d are indicated by arrows. **f** Dipole field along the *z*-direction near grains A and B indicated in **e**.

$\Delta\theta_i + \Delta\theta_{i,1}$ owing to the dipolar and exchange interactions. In contrast with the easy-axis tilt angle, the diameter of the grains does not relate to the generation of magnetization reversal regions. The correlation coefficients for the diameter and $\Delta\theta_i + \Delta\theta_{i,1}$ are 0.21 and −0.67, respectively. The correlation coefficient for $\Delta\theta_i + \Delta\theta_{i,1}$ represents a negative correlation.

In this study, the effects of contacted grains on the correlation coefficients pertaining to the maximum dipole field and grain switching time were considered. Figure 6a shows the correlation coefficient pertaining to the maximum dipole field as a function of $\Delta\theta_i + \sum_{k=1}^{n} \Delta\theta_{i,k}$. As observed, this correlation coefficient is not significantly increased by considering $\Delta\theta_{i,2}$ and $\Delta\theta_{i,3}$—defined as the second- and third-largest easy-axis tilt angles with respect to the *z*-axis, as shown Fig. 4d. Although the correlation coefficient slightly increases when considering $\Delta\theta_{i,2}$ and $\Delta\theta_{i,3}$, its value remains small. Figure 6b shows the absolute values of the correlation coefficient between the switching time of the grains and $\Delta\theta_i + \sum_{k=1}^{n} \Delta\theta_{i,k}$.

The correlation coefficient increases by 0.1 when considering the effect of the contacted grains with the second- or third-largest easy-axis tilt angles. Thus, contrary to the dipole field, the easy-axis tilt angles of grains represent the initiation of magnetic nucleation inside permanent magnets. Tilting of the easy axes of grains does not always increase the dipole field, as can be seen in Fig. 4e. However, tilted easy axes are indispensable for the generation of strong dipole fields. Thus, the easy axes of grains can be used to identify grains wherein initiation of magnetic nucleation occurs.

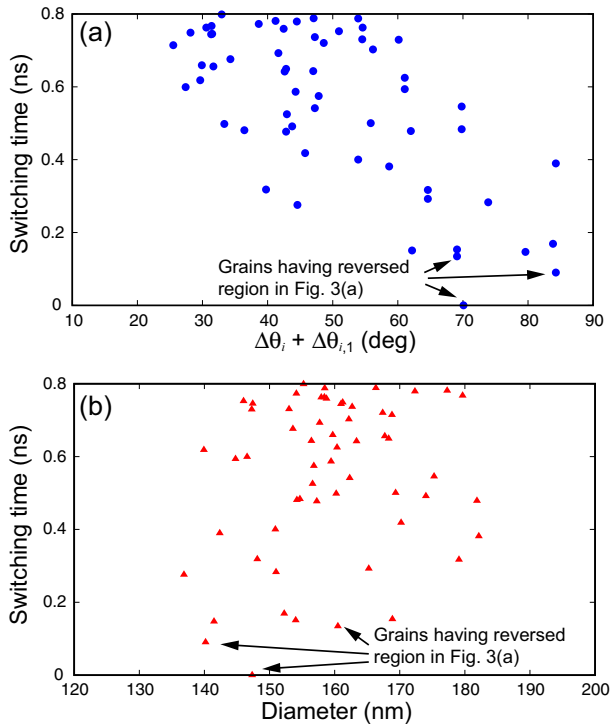

Fig. 5 Switching times in grain. Relationship of the switching time when the total magnetization in individual grains vanishes with **a** $\Delta\theta_i+\Delta\theta_{i,1}$ and **b** the diameter of the grain. Blue circles (red triangles) represent the relationship with $\Delta\theta_i+\Delta\theta_{i,1}$ (the diameter). Grains that have a magnetization reversal region in Fig. 2d are indicated by the arrows.

The results of this study suggest that the magnetization reversal process can be represented by the microstructure of the permanent magnet. The easy-axis orientations describe the grains in which magnetization reversal is initiated, and a concentration of grains with tilted easy axes reduces the coercivity owing to the nucleation of magnetization reversal. In this analysis, it is unnecessary to use the magnetization information inside the permanent magnet. This study provides a method to improve the coercivity of the permanent magnet by avoiding the concentration of grains with tilted easy axes and a method to analyze the performance of a permanent magnet without large-scale micromagnetic simulations. The correlations in Figs. 4e, 5a, and 6 are not as strong because the local dipole field is influenced by other structures of the permanent magnet, such as the azimuthal angle of the easy axis and the distribution of the dipole field in the xy-plane. In future work, we will clarify the effects of other structures, including grain boundary phases, on magnetization reversal.

Summary

The origin of magnetic nucleation inside hot-deformed permanent magnets was clarified by performing a large-scale micromagnetics simulation considering 3391 tabular grains whose diameters and easy-axis orientations have distributions. The magnetization reversal process starts when the external field reaches the coercivity. After nucleation of magnetization reversal, the domain walls displace across the grain boundaries, and the magnetization reversal region expands into the hot-deformed permanent magnet. The magnetization reversal region has a

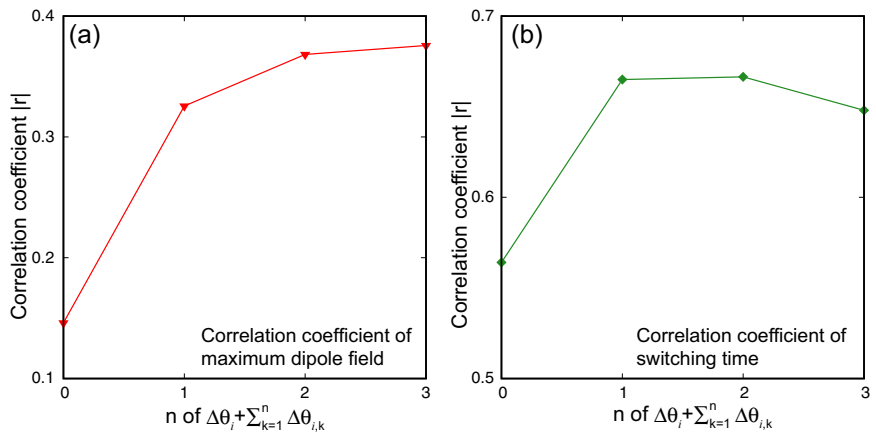

Fig. 6 Correlation coefficients. Absolute values of the correlation coefficients of **a** the maximum dipole field and **b** the switching time as a function of $\Delta\theta_i+\sum_{k=1}^{n}\Delta\theta_{i,k}$.

pillar-like structure owing to the dipolar interaction, which tends to move the domain wall in a direction parallel to the external field. At the coercivity, our simulation reproduces the interaction domain structure, in which the single-domain grains construct the domain structure.

The dipole field promotes the nucleation of magnetization reversal. The dipole field has a distribution inside the permanent magnet, and its absolute value reaches 1.76 T at the region where the magnetization reversal initiates. In contrast, the exchange and anisotropy fields do not have local distributions inside the grains. The switching field of the grain in which magnetization reversal is initiated is almost the same as the sum of the external field and the dipole field.

The dipole fields inside permanent magnet models do not have a relationship with the easy-axis orientations of the constituent grains. Thus, the dipole field in permanent magnets cannot be described only by these easy-axis orientations owing to the complex overlapping of grains. However, contrary to the dipole field, magnetic nucleation has a strong correlation with the easy-axis tilt angles of grains. Since tilted easy-axis orientations are necessary for the generation of a dipole field, grains wherein magnetic nucleation initiates can be identified based on their easy-axis tilt angles. The results of this study suggest the possibility of identifying the grain in which magnetization reversal starts by using the microstructure of the permanent magnet and provide a method to enhance the coercivity by avoiding the concentration of grains with tilted easy axes.

Acknowledgements
This work was in part supported by the Elements Strategy Initiative Center for Magnetic Materials (ESICMM), Grant Number JPMXP0112101004, through the Ministry of Education, Culture, Sports, Science and Technology (MEXT). We gratefully acknowledge the financial support by Toyota Motor Corporation. The supercomputer simulations were performed by the Large Scale Simulation Program 15/16–18 of the High Energy Accelerator Research Organization (KEK). The authors would like to express their sincere thanks to the crew of the Center for Computational Materials Science of the Institute for Materials Research, Tohoku University, for their continuous support of the supercomputing facilities.

Author contributions
H.T. performed calculations and data analysis and participated in the writing of the paper. H.T., K.I., T.I., and C.M. discussed the results of the paper. K.O. supervised this research and participated in the writing of the paper.

Conflict of interest
The authors declare that they have no conflict of interest.

Publisher's note
Springer Nature remains neutral with regard to jurisdictional claims in published maps and institutional affiliations.

Received: 29 August 2019 Revised: 27 January 2020 Accepted: 18 February 2020.
Published online: 17 April 2020

References
1. Lee, R. W. Hot-pressed neodymium-iron-boron magnets. *Appl. Phys. Lett.* **46**, 790–791 (1985).
2. Lee, R. W., Brewer, E. G. & Schaffel, N. A. Processing of neodymium-iron-boron melt-spun ribbons to fully dense magnets. *IEEE Trans. Magn.* **21**, 1958–1963 (1985).
3. Mishra, R. K. & Lee, R. W. Microstructure, domain walls, and magnetization reversal in hot-pressed Nd-Fe-B magnets. *Appl. Phys. Lett.* **48**, 733–735 (1986).
4. Mishra, R. K., Chu, T. -Y. & Rabenberg, L. K. The development of the microstructure of die-upset Nd-Fe-B magnets. *J. Magn. Magn. Mater.* **84**, 88–94 (1990).
5. Mishra, R. K., Brewer, E. G. & Lee, R. W. Grain growth and alignment in hot deformed Nd-Fe-B magnets. *J. Appl. Phys.* **63**, 3528–3530 (1988).
6. Mishra, R. K. Microstructure of hot-pressed and die-upset NdFeB magnets. *J. Appl. Phys.* **62**, 967–971 (1987).
7. Gopalam, R. et al. Anisotropic Nd-Fe-B nanocrystalline magnets processed by spark plasma sintering and in situ hot pressing of hydrogenation-decomposition-desorption-recombination powder. *Scr. Mater.* **61**, 978–981 (2009).
8. Sepehri-Amin et al. Enhancement of coercivity of hot-deformed Nd-Fe-B anisotropic magnet by low-temperature grain boundary diffusion of $Nd_{60}Dy_{20}Cu_{20}$ eutectic alloy. *Scr. Mater.* **69**, 647–650 (2013).
9. Sepehri-Amin, H. et al. Microstructure and temperature dependent of coercivity of hot-deformed Nd-Fe-B magnets diffusion processed with Pr-Cu alloy. *Acta Mater.* **99**, 297–306 (2015).
10. Kronmüller, H., Durst, K.-D. & Sagawa, M. Analysis of the magnetic hardening mechanism in RE-FeB permanent magnets. *J. Magn. Magn. Mater.* **74**, 291–302 (1988).
11. Liu, J. et al. Effect of Nd content on the microstructure and coercivity of hot-deformed Nd-Fe-B permanent magnets. *Acta Mater.* **61**, 5387–5399 (2013).
12. Takezawa, M., Kimura, Y., Morimoto, Y. & Yamasaki, J. Analysis of magnetization reversal process of Nd-Fe-B sintered magnets by magnetic domain observation using Kerr microscope. *IEEE Trans. Magn.* **49**, 3262–3264 (2013).
13. Takezawa, M., Ogimoto, H., Kimura, Y. & Morimoto, Y. Analysis of the demagnetization process of Nd-Fe-B sintered magnets at elevated temperatures by magnetic domain observation using a Kerr microscope. *J. Appl. Phys.* **115**, 17A733 (2014).
14. Suzuki, M. et al. Magnetic domain evolution in Nd-Fe-B:Cu sintered magnet visualized by scanning hard X-ray microprobe. *Acta Mater.* **106**, 155–161 (2016).
15. Soderžnik, M. et al. Magnetization reversal of exchange-coupled and exchange-decoupled Nd-Fe-B magnets observed by magneto-optical Kerr effect microscopy. *Acta Mater.* **135**, 68–76 (2017).
16. Livingston, J. D. A review of coercivity mechanisms. *J. Appl. Phys.* **52**, 2544–2548 (1981).
17. Givord, D., Rossignol, M. & Taylor, D. Coercivity mechanisms in hard magnetic materials. *J. Phys. IV* **C3**, 95–104 (1992).
18. Fischer, R. & Kronmüller, H. Static computational micromagnetism of demagnetization processes in nanoscaled permanent magnets. *Phys. Rev. B* **54**, 7284–7294 (1996).
19. Woodcock, T. G. et al. Understanding the microstructure and coercivity of high performance NdFeB-based magnets. *Scr. Mater.* **67**, 536–541 (2012).
20. Hilzinger, H.-R. & Kronmüller, H. Investigation of bloch-wall-pinning by antiphase boundaries in RCo5-compounds. *Phys. Lett. A* **51**, 59–60 (1975).
21. Friedberg, R. & Paul, D. I. New theory of coercive force of ferromagnetic materials. *Phys. Rev. Lett.* **34**, 1234–1237 (1975).
22. Kronmüller, H. & Hilzinger, H. R. Incoherent nucleation of reversed domains in Co_5Sm permanent magnets. *J. Magn. Magn. Mater.* **2**, 3–10 (1976).
23. Kronmüller, H. Micromagnetism in hard magnetic materials. *J. Magn. Magn. Mater.* **7**, 341–350 (1978).
24. Kronmüller, H. & Goll, D. Micromagnetic theory of the pinning of domain walls at phase boundaries. *Physica B* **319**, 122–126 (2002).
25. Rong, C. B., Zhang, H. & Chen, R. J. The role of dipolar interaction in nanocomposite permanent magnets. *J. Magn. Magn. Mater.* **302**, 126–136 (2006).
26. Kronmüller, H., Durst, K. -D. & Martinek, G. Angular dependence of the coercive field in sintered $Fe_{77}Nd_{15}B_8$ magnets. *J. Magn. Magn. Mater.* **69**, 149–157 (1987).
27. Gao, R. W. et al. Coercivity and its dependence on the strength of alignment magnetic field in Nd-Fe-B sintered magnets. *J. Appl. Phys.* **78**, 1156–1159 (1995).

28. Gao, R. W. & Zhang, D. H. Effect of grain alignment on the coercivity for sintered NdFeB magnets. *Jpn. J. Appl. Phys.* **35**, 4628–4632 (1996).
29. Gao, R. W., Li, W., Zhang, J., Wu, L. & Yu, X. Effects of orientation and interaction of grains on coercivity for sintered NdFeB magnets. *Sci. China Ser. A* **42**, 653–659 (1999).
30. Schrefl, T., Schmidts, H. F., Filder, J. & Kromuller, H. The role of exchange and dipolar coupling at grain boundaries in hard magnetic materials. *J. Magn. Magn. Mater.* **124**, 251–261 (1993).
31. Schrefl, T., Fidler, J. & Kromuller, H. Nucleation fields of hard magnetic particles in 2D and 3D micromagnetic calculations. *J. Magn. Magn. Mater.* **138**, 15–30 (1994).
32. Schrefl, T., Fidler, J. & Kronmüller, H. Remanence and coercivity in isotropic nanocrystalline permanent magnets. *Phys. Rev. B* **49**, 6100–6110 (1994).
33. Fischer, R., Schrefl, T., Kronmüller, H. & Fidler, J. Grain-size dependence of remanence and coercive field of isotropic nanocrystalline composite permanent magnets. *J. Magn. Magn. Mater.* **153**, 35–49 (1996).
34. Rave, W. & Ramstöck, K. Micromagnetic calculation of the grain size dependence of remanence and coercivity in nanocrystalline permanent magnets. *J. Magn. Magn. Mater.* **171**, 69–82 (1997).
35. Fidler, J. & Schrefl, T. Micromagnetic modelling—the current state of the art. *J. Phys. D* **33**, R135–R156 (2000).
36. Lee, S. -J., Sato, S., Yanagihara, H., Kita, E. & Mitsumata, C. Numerical simulation of random magnetic anisotropy with solid magnetization grains. *J. Magn. Magn. Mater.* **323**, 28–31 (2011).
37. Fujisaki, J. et al. Micromagnetic simulations of magnetization reversal in misaligned multigrain magnets with various grain boundary properties using large-scale parallel computing. *IEEE Trans. Magn.* **50**, 7100704 (2014).
38. Tsukahara, H., Iwano, K., Mitsumata, C., Ishikawa, T. & Ono, K. Magnetization reversal processes of isotropic permanent magnets with various inter-grain exchange interactions. *AIP Adv.* **7**, 056224 (2017).
39. Tsukahara, H., Iwano, K., Mitsumata, C., Ishikawa, T. & Ono, K. Micromagnetic simulation for the magnetization reversal process of Nd-Fe-B hot-deformed nanocrystalline permanent magnets. *AIP Adv.* **7**, 056234 (2017).
40. Tsukahara, H., Iwano, K., Ishikawa, T., Mitsumata, C. & Ono, K. Large-scale micromagnetics simulation of magnetization dynamics in a permanent magnet during the initial magnetization process. *Phys. Rev. Appl.* **11**, 014010 (2019).
41. Erokhin, S., Berkov, D., Gorn, N. & Michels, A. Micromagnetic modeling and small-angle neutron scattering characterization of magnetic nanocomposites. *Phys. Rev. B* **85**, 024410 (2012).
42. Berkov, D. V. & Gorn, N. L. *Handbook of Advanced Magnetic Materials*, Vol. 2, 794–880 (Springer, US, 2006).
43. Tsukahara, H., Iwano, K., Mitsumata, C., Ishikawa, T. & Ono, K. Effect of grain boundary phase on the magnetization reversal process of nanocrystalline magnet using large-scale micromagnetic simulation. *AIP Adv.* **8**, 056226 (2018).
44. Nakatani, Y., Uesaka, Y. & Hayashi, N. Direct solution of the Landau-Lifshitz-Gilbert equation for micromagnetics. *Jpn. J. Appl. Phys.* **28**, 2485–2507 (1989).
45. Fukushima, H., Nakatani, Y. & Hayashi, N. Volume average demagnetizing tensor of rectangular prisms. *IEEE Trans. Magn.* **34**, 193–198 (1998).
46. Tsukahara, H., Iwano, K., Mitsumata, C., Ishikawa, T. & Ono, K. Implementation of low communication frequency 3D FFT algorithm for ultra-large-scale micromagnetics simulation. *Comput. Phys. Commun.* **207**, 217–220 (2016).
47. Fehlberg, E. Low-order classical Runge-Kutta formulas with stepsize control and their application to some heat transfer problems, *NASA Technical Report* R-315 (Washington, US, 1969).
48. Romeo, A. et al. A numerical solution of the magnetization reversal modeling in a permalloy thin film using fifth order Runge–Kutta method with adaptive step size control. *Physica B* **403**, 464–468 (2008).
49. Croat, J. J., Herbst, J. F., Lee, R. W. & Pinkerton, F. E. Nonanomalous energy distribution of electrons emitted by a thermionic cathode. *Appl. Phys. Lett.* **44**, 148–149 (1984).
50. Croat, J. J., Herbst, J. F., Lee, R. W. & Pinkerton, F. E. Pr-Fe and Nd-Fe-based materials: a new class of high-performance permanent magnets. *J. Appl. Phys.* **55**, 2078–2082 (1984).
51. Sagawa, M., Fujimura, S., Togawa, N., Yamamoto, H. & Matsuura, Y. New material for permanent magnets on a base of Nd and Fe. *J. Appl. Phys.* **55**, 2083–2087 (1984).
52. Okuda, M., Sugimoto, S., Ishizaka, C., Tanaka, T. & Homma, M. Didymium-Fe-B sintered permanent magnets. *J. Appl. Phys.* **57**, 4146–4148 (1985).
53. Sagawa, M., Fujimura, S., Yamamoto, H., Matsuura, Y. & Hirosawa, S. Magnetic properties of rare-earth-iron-boron permanent magnet materials. *J. Appl. Phys.* **57**, 4094–4096 (1985).
54. Schrefl, T. & Fidler, J. Micromagnetic simulation of magnetizability of nanocomposite Nd-Fe-B magnets. *J. Appl. Phys.* **83**, 6262–6264 (1998).
55. Inami, N. et al. Three-dimensional large-scale micromagnetics simulation using Fast Fourier transformation. *IEEE Trans. Magn.* **50**, 1400304 (2013).
56. Tsukahara, H. et al. Large-scale micromagnetics simulations with dipolar interaction using all-to-all communications. *AIP Adv.* **6**, 056405 (2016).
57. Ohtori, H. et al. Dipolar energy of Nd-Fe-B nanocrystalline magnets in magnetization reversal process. *J. Appl. Phys.* **115**, 17A717 (2014).
58. Ohtori, H. et al. Dipolar energies in Nd-Fe-B nanocrystalline magnets with and without Nd-Cu infiltration. *J. Appl. Phys.* **117**, 17B312 (2015).
59. Stoner, E. C. & Wohlfarth, E. P. A mechanism of magnetic hysteresis in heterogeneous alloys. *Philos. Trans. R. Soc.* **A240**, 599–644 (1948).